electronics

MDPI

Article

Interference of Spread-Spectrum EMI and Digital Data Links under Narrowband Resonant Coupling

Paolo Stefano Crovetti *,† and Francesco Musolino †

Department of Electronics and Telecommunications (DET), Politecnico di Torino, 10129 Turin, Italy; francesco.musolino@polito.it
* Correspondence: paolo.crovetti@polito.it; Tel.: +39-011-090-4220
† The authors contributed equally to this work.

Received: 6 November 2019; Accepted: 17 December 2019; Published: 1 January 2020

Abstract: In this paper, the effects of electromagnetic interference (EMI) coupled to a radio-frequency (RF) communication channel by resonant mechanisms are investigated and described in the framework of Shannon information theory in terms of an equivalent channel capacity loss so that to analyze and compare the effects of non-modulated and random Spread Spectrum (SS) modulated EMI. The analysis reveals a higher EMI-induced capacity loss for SS-modulated compared to non modulated EMI under practical values of the quality factor Q, while a modest improvement in the worst case capacity loss is observed only for impractical values of Q. Simulations on a 4-quadrature amplitude modulation (4-QAM) digital link featuring Turbo coding under EMI resonant coupling reveal that SS-modulated EMI gives rise to higher bit error rate (BER) at lower EMI power compared non-modulated EMI in the presence of resonant coupling for practical values of Q, thus suggesting a worse interfering potential of SS-modulated EMI.

Keywords: Spread Spectrum; DC–DC power converters; digital communications; channel capacity; resonant coupling

1. Introduction

Due to the widespread diffusion of highly integrated information and communication technology (ICT) systems like smartphones, tablets and intelligent sensor nodes, digital communication modules operate in a more and more harsh electromagnetic environment, in which electromagnetic interference (EMI) from digital integrated circuits (ICs) and switching mode power converters can be easily coupled to the nominal signal path via the silicon substrate, the IC package and the power distribution network of ICs and printed circuit boards (PCBs), resulting in a degraded bit error rate (BER) and possibly in a complete communication failure [1–7].

As a consequence, the effects of EMI need to be addressed adopting specific countermeasures as early as possible in the design of circuits and systems and/or by limiting the coupling mechanisms so that to assure the proper operation with no penalty in terms of costs, time-to-market and performance, and also in order to meet the stringent Electromagnetic Compatibility (EMC) regulations [8–11].

For this purpose, several approaches have been proposed in recent years to mitigate EMI [12–16]. Among them, *Spread-Spectrum (SS) techniques*, which consist in the modulation of the frequency of switching signals around the nominal value, so that to spread their spectral energy over a wider bandwidth [17,18], are often adopted in clock oscillators [19–23] and DC–DC converter controllers [24–27] since they give rise to a significant (10–20 dB) reduction of EMI spectral peaks measured following EMC standards [8–11] and make it possible to meet EMC requirements at low cost. In this field, chaos-based random SS-modulations have proven to achieve the best spectral characteristics [28–30].

While SS techniques help in complying with EMC regulations, their effectiveness in reducing the interfering potential of switching signals is more controversial and has been sometimes put in question [31–34]. Moreover, SS-modulations have found to bring no BER reduction in an I^2C link operating in the presence of EMI generated by a power converter [35] and a worse interfering potential of SS-modulated compared to non-modulated EMI in Wireless Local Area Networks (WLAN) is reported in [36].

In this scenario, focusing on the effects of SS EMI on digital communications, the impact of random SS-modulated interference on baseband digital data lines has been described in [37] in terms of an equivalent channel capacity loss and compared with non-SS-modulated EMI in practical application scenarios, revealing that SS-modulated EMI can show a worse interfering potential compared to non-modulated EMI in a digital link featuring advanced channel coding. The analysis presented in [37], however, was carried out assuming frequency-independent EMI coupling in the victim channel bandwidth. This assumption conveniently describes low frequency inductive and capacitive coupling scenarios in baseband data links but could not be valid in general in the presence of radiated and conducted EMI resonant coupling mechanisms [38–42], which affect high-frequency EMI propagation and can be therefore relevant when interference with radio-frequency (RF) digital communications are considered.

Generally speaking, in the presence of resonant coupling, the adoption of SS-modulations may lead to a more significant reduction of the EMI power which is actually coupled to the victim equipment compared with the case of wideband coupling considered in [37], as illustrated in Figure 1, where B and W are the channel and the EMI bandwidth, respectively. From the figure, it can be observed that under the same resonant coupling mechanism $G(f)$, the coupled EMI power can be reduced of more than 50% by adopting SS-modulations compared to the non-SS-modulated case. In this paper the analysis in [37] is extended to investigate if and to what extent the conclusions on the worse EMI-induced capacity loss of SS-modulated signals presented in [37] apply to the case of resonant coupling.

The paper is organized as follows: in Section 2, the model of a digital communication channel under EMI resonant coupling is introduced. With reference to such a model, a description of the adverse effects of EMI in terms of capacity loss is introduced in Section 3 and discussed in Section 4. Simulations on the effects of resonant-coupled EMI from a switching mode DC—DC converter on a 4-quadrature amplitude modulation (4-QAM) data link featuring Turbo coding are then presented in Section 5 to verify the theoretical results with reference to a practical case. Finally, in Section 6, some concluding remarks are drawn.

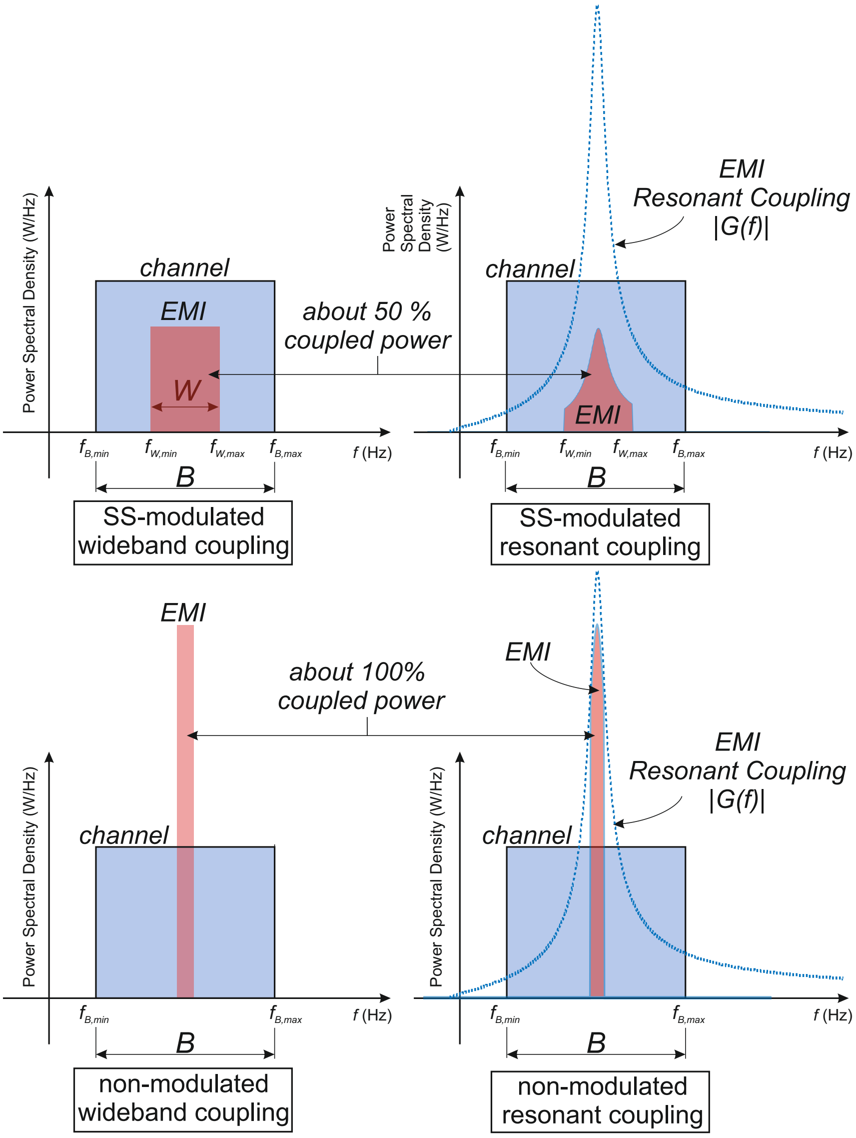

Figure 1. Effects of resonant coupling mechanisms on non-modulated and SS-modulated EMI.

2. Communication Channel Modeling under Resonant EMI Coupling

In this paper, the interfering potential of periodic and SS-modulated EMI generated by switching signals and coupled to a digital communication channel by a resonant coupling mechanism, as depicted in Figure 2, are compared in the framework of Shannon information theory in terms of an equivalent EMI-induced channel capacity loss [43], following the approach adopted in [37].

2.1. Channel Modelling

A band-limited communication channel corrupted by additive white Gaussian noise (AWGN) with unilateral power spectral density N_0 is considered in what follows. The transmitted signal and the background noise are both described by two wide-sense stationary (WSS), statistically independent gaussian random processes. In particular, the signal process is assumed to have a total power P_S and a power spectral density (p.s.d.) P_S/B constant over the channel bandwidth $B = \left(f_{B_{\min}}, f_{B_{\max}}\right)$, as depicted in Figure 3, while the noise is assumed to have unilateral power spectral density N_0.

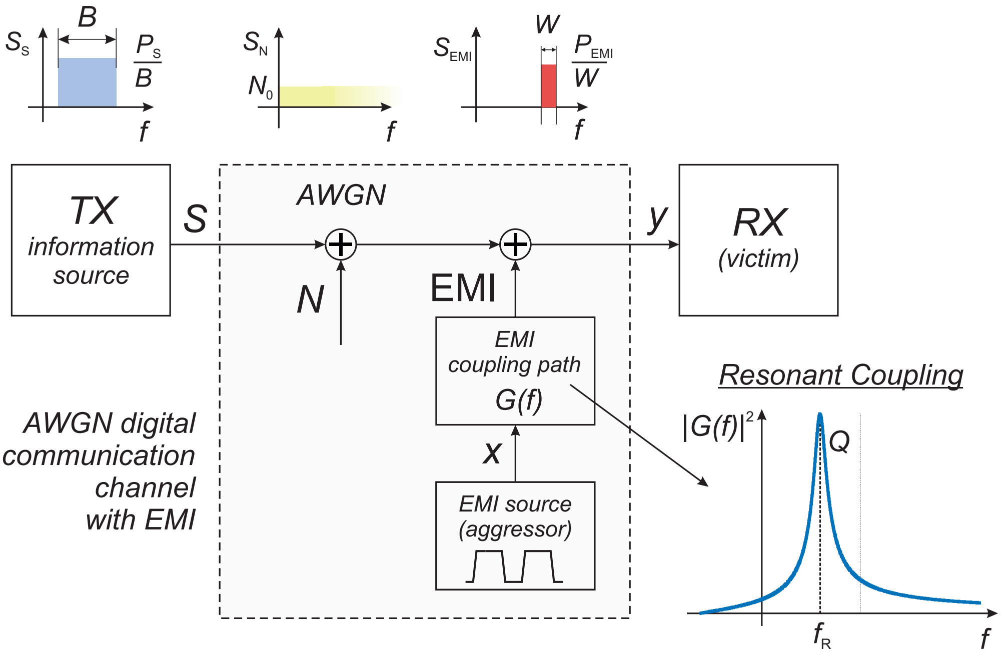

Figure 2. Digital communication channel with EMI resonant coupling: Block Diagram.

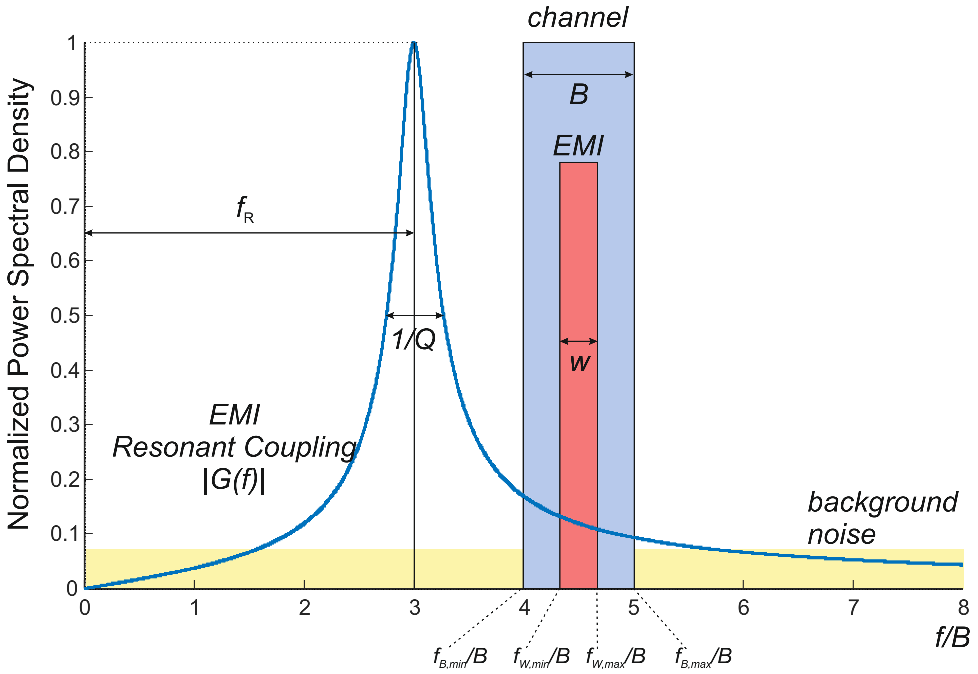

Figure 3. EMI resonant coupling in the frequency domain: power spectral densities of nominal signals, EMI, background noise and resonant coupling transfer function.

In the framework of Shannon information theory, the upper bound of the information than can be reliably transmitted over the AWGN channel considered above in the unit time, is given by the Shannon-Hartley equation [43]:

$$C_0 = B \log_2 \left(1 + \frac{P_S}{BN_0} \right) = B \log_2 (1 + \alpha) \tag{1}$$

where

$$\alpha = \frac{P_S}{BN_0}$$

is the signal-to-noise ratio (SNR) of the AWGN channel.

2.2. Modelling of a Communication Channel Affected by EMI

In the above model, it is now assumed that the communication channel is also corrupted by EMI generated by an aggressor whose operation is based on periodic or randomly SS-modulated switching signals.

In case of periodic signals, the EMI spectrum has nonzero components only at the harmonics kf_0, with $k \in \mathbb{N}$, of the switching frequency f_0 of the aggressor. By contrast, when SS techniques are applied, the instantaneous frequency f of the aggressor varies according to the law

$$f(t) = f_0 + \delta f_0 \xi(t) \tag{2}$$

where f_0 is the central frequency, δ is the modulation depth and $0 \leq \xi(t) \leq 1$ is the modulation profile. As a consequence, the EMI spectral power is more or less uniformly spread over the bandwidth $[kf_0, kf_0(1+\delta)]$ and the spectral peaks are consequently reduced. By using SS-modulations with a random modulation profile $\xi(t)$ optimized for this purpose, the EMI power can be effectively spread over the whole spreading bandwidth $[kf_0, kf_0(1+\delta)]$ in a nearly uniform way, leading to a reduction of the EMI p.s.d. to $P_k/k\delta f_0$ which makes it easier to comply with EMC regulations.

Under the above hypotheses, EMI around an harmonic kf_0 within the bandwidth B of the communication channel in Figure 2 is modelled by a wide-sense stationary (WSS) narrowband Gaussian process, independent both of the background noise and of the transmitted signal, with total power P_{EMI} and bandwidth W, completely or partially overlapping the signal bandwidth B.

2.3. Resonant Coupling Modeling

Even if realistic EMI coupling transfer functions can be rather complex depending on the specific physical mechanism involved in conducted/radiated EMI propagation, focusing the attention to the relatively narrow region of the spectrum included in the bandwidth of the victim channel, practical resonant coupling mechanisms can be conveniently described by a second-order resonant transfer function:

$$G(f) = G_0 \frac{\frac{\jmath f}{Q f_{\text{R}}}}{1 + \frac{\jmath f}{Q f_{\text{R}}} - \frac{f^2}{f_{\text{R}}^2}} \tag{3}$$

where G_0 is a frequency-independent coupling factor, f_{R} is the resonance frequency and Q is the quality factor.

In view of that, for the sake of simplicity and without loss of generality, the effects of resonant EMI coupling on the EMI-induced capacity loss will be discussed in the following considering the EMI transfer function $G(f)$ in (3).

3. EMI-Induced Channel Capacity Loss

Under the hypotheses introduced in the previous Section, the capacity C of a communication channel in the presence of EMI, for a single EMI harmonic overlapping completely or in part with the channel bandwith B, as depicted in Figure 3 can be calculated as

$$C = C_1 + C_2 \tag{4}$$

where C_1 is the capacity of sub-channel where the signal bandwidth overlaps with the EMI bandwidth, i.e., over the bandwidth

$$W^\star = B \bigcap W = [W^\star_{\text{min}}, W^\star_{\text{max}}] = \left[\max\left(f_{B_{\text{min}}}, f_{W_{\text{min}}}\right), \min\left(f_{B_{\text{max}}}, f_{W_{\text{max}}}\right)\right]. \tag{5}$$

and can be expressed as

$$C_1 = \int_{W^\star} \log_2 \left(1 + \frac{S_\mathrm{S}(f)}{S_\mathrm{N}(f) + |G(f)|^2 S_\mathrm{EMI}(f)} \right) \mathrm{d}f \tag{6}$$

where:

$$S_\mathrm{S}(f) = \frac{P_\mathrm{S}}{B} \Pi_B(f - f_\mathrm{B,min})$$

is the signal p.s.d.,

$$S_\mathrm{N}(f) = N_0$$

is the background noise p.s.d.,

$$S_\mathrm{EMI}(f) = \frac{P_\mathrm{EMI}}{W} \Pi_W(f - f_\mathrm{W,min})$$

is the EMI p.s.d. and $G(f)$ is the resonant coupling transfer function defined in (3).

By introducing in (6) the expressions of $S_\mathrm{S}(f)$, $S_\mathrm{N}(f)$ and $G(f)$ derived above, the capacity of the sub-channel C_1 affected by EMI can be explicitly evaluated as

$$\begin{aligned} C_1 &= \int_{B \bigcap W} \log_2 \left(1 + \frac{S_\mathrm{S}(f) \left[1 + \left(\frac{1}{Q^2} - 2 \right) \frac{f^2}{f_\mathrm{R}^2} + \frac{f^4}{f_\mathrm{R}^4} \right]}{S_\mathrm{N}(f) + \left[S_\mathrm{N}(f) \left(\frac{1}{Q^2} - 2 \right) + \frac{G_0^2}{Q^2} S_\mathrm{EMI}(f) \right] \frac{f^2}{f_\mathrm{R}^2} + S_\mathrm{N}(f) \frac{f^4}{f_\mathrm{R}^4}} \right) \mathrm{d}f \\ &= \int_{B \bigcap W} \log_2 \left(1 + \frac{P_\mathrm{S}}{B N_0} \frac{1 + \left(\frac{1}{Q^2} - 2 \right) \frac{f^2}{f_\mathrm{R}^2} + \frac{f^4}{f_\mathrm{R}^4}}{1 + \left(\frac{1}{Q^2} - 2 + G_0 \frac{P_\mathrm{EMI}}{W N_0} \right) \frac{f^2}{f_\mathrm{R}^2} + \frac{f^4}{f_\mathrm{R}^4}} \right) \mathrm{d}f \\ &= \int_{B \bigcap W} \log_2 \left(1 + \alpha \frac{1 + \left(\frac{1}{Q^2} - 2 \right) \frac{f^2}{f_\mathrm{R}^2} + \frac{f^4}{f_\mathrm{R}^4}}{1 + \left(\frac{1}{Q^2} - 2 + \alpha\beta \right) \frac{f^2}{f_\mathrm{R}^2} + \frac{f^4}{f_\mathrm{R}^4}} \right) \mathrm{d}f \\ &= \int_{B \bigcap W} \log_2 (1 + \alpha) + \log_2 \left(\frac{1 + a_1 \frac{f^2}{f_\mathrm{R}^2} + \frac{f^4}{f_\mathrm{R}^4}}{1 + a_2 \frac{f^2}{f_\mathrm{R}^2} + \frac{f^4}{f_\mathrm{R}^4}} \right) \mathrm{d}f \end{aligned} \tag{7}$$

where

$$a_1 = \frac{\frac{1}{Q^2} - 2 + \alpha\,(\beta + 1)}{1 + \alpha},$$

$$a_2 = \frac{1}{Q^2} - 2 + \alpha\beta$$

and where α is the signal-to-noise ratio as in (1) and $\beta = P_\mathrm{EMI}/P_\mathrm{S}$ is the overall EMI-to-signal power ratio. Since the integral in (7) can be calculated analytically in closed form in terms of:

$$\begin{aligned} \Theta(x, a) &= \int \log_2 \left(x^2 + a\,x + 1 \right) \mathrm{d}x \\ &= \frac{1}{\log 2} \left[\left(x + \frac{a}{2} \right) \log \left(x^2 + ax + 1 \right) - 2x + \sqrt{4 - a^2} \arctan \frac{2x - a}{\sqrt{4 - a^2}} \right] \end{aligned} \tag{8}$$

the capacity C_1 can be finally expressed as

$$C_1 = \tfrac{W^\star}{B} C_0 + \Theta\left[\left(\tfrac{W^*_\mathrm{max}}{f_\mathrm{R}} \right)^2, a_1 \right] - \Theta\left[\left(\tfrac{W^*_\mathrm{min}}{f_\mathrm{R}} \right)^2, a_1 \right] - \Theta\left[\left(\tfrac{W^*_\mathrm{max}}{f_\mathrm{R}} \right)^2, a_2 \right] + \Theta\left[\left(\tfrac{W^*_\mathrm{min}}{f_\mathrm{R}} \right)^2, a_2 \right] \tag{9}$$

where C_0 is the capacity of the EMI-free channel.

With the same notations, the capacity C_2 of the complementary sub-channel $B - B \bigcap W$, not affected by EMI, can be expressed as

$$\begin{aligned} C_2 &= \int_{B - B \bigcap W} \log_2 \left(1 + \frac{S_S(f)}{N_0}\right) \mathrm{d}f \\ &= (B - W^\star) \log_2 (1 + \alpha) = \left(1 - \frac{W^\star}{B}\right) C_0. \end{aligned} \tag{10}$$

Replacing (7) and (10) in (4), the overall channel capacity in the presence of EMI can be expressed in the form

$$C = C_0 + \Delta C \tag{11}$$

where

$$\Delta C = \Theta\left[\left(\frac{W^*_{\mathrm{max}}}{f_{\mathrm{R}}}\right)^2, a_1\right] - \Theta\left[\left(\frac{W^*_{\mathrm{min}}}{f_{\mathrm{R}}}\right)^2, a_1\right] - \Theta\left[\left(\frac{W^*_{\mathrm{max}}}{f_{\mathrm{R}}}\right)^2, a_2\right] + \Theta\left[\left(\frac{W^*_{\mathrm{min}}}{f_{\mathrm{R}}}\right)^2, a_2\right] \tag{12}$$

is the channel capacity loss due to the presence of EMI.

The analysis presented so far can be applied to calculate the capacity loss ΔC_k in an AWGN channel due to EMI at frequency kf_0 with up-spreading, symmetric and down-spreading SS-modulations and modulation depth δ, by considering $W = \delta k f_0$ and appropriate values of $W^\star_{\mathrm{min}}$ and $W^\star_{\mathrm{max}}$ in (12) by the same approach detailed in [37]. Moreover, the EMI-induced capacity loss ΔC_{TOT} due to several non-overlapping EMI spectral lines can be immediately evaluated by superposition of the capacity loss contributions due to each spectral line $k = N_1 \ldots N_2$ in the channel bandwidth as

$$\Delta C_{\mathrm{TOT}} = \sum_{k=N_1}^{N_2} \Delta C_k. \tag{13}$$

4. Discussion

Based on the results presented in Section 3, the effects of SS-modulation under resonant EMI coupling are now investigated and discussed.

For this purpose, a bandpass channel with bandwidth B ranging from $f_{B_{\mathrm{min}}} = 4B$ to $f_{B_{\mathrm{max}}} = 5B$ is considered and an aggressor generating periodic or random SS-modulated EMI with a fixed total power 20dB below the total signal power, concentrated in a spectral line at frequency f_0 falling in correspondence of the central frequency of the channel $f_C = \frac{f_{B_{\mathrm{min}}} + f_{B_{\mathrm{max}}}}{2} = f_0 = 4.5B$ is considered, as depicted in Figure 4. The signal-to-background noise ratio of the channel is assumed to be 47dB so that the background thermal noise is negligible compared to EMI.

Moreover, it is assumed that the EMI source is coupled to the victim receiver by a resonant coupling function $G(f)$ in (3), with resonant frequency f_{R} and quality factor Q, where the scaling constant G_0 is chosen so that to have unity peak amplitude

$$\max_f |G(f)| = 1.$$

The channel capacity is evaluated accordingly as in Section 3 and is plotted in Figure 4 for $Q = 100$ versus the resonant frequency f_{R} and for different values of the SS EMI bandwidth W normalized with respect to the channel bandwidth B, for W/B ranging from 0 (no SS) up to 25%. Based on (2), depending on the EMI harmonic order k, the SS-modulation depth can be expressed in terms of the normalized bandwidth W/B as

$$\delta = \frac{W}{kf_0} = \frac{W}{B} \frac{1}{4.5 \cdot k}. \tag{14}$$

The same analysis is repeated in Figure 5 for different values of the quality factor Q ranging from 1 to 1,000,000 to discuss the effects of SS-modulations on signal capacity under different resonant coupling quality factors.

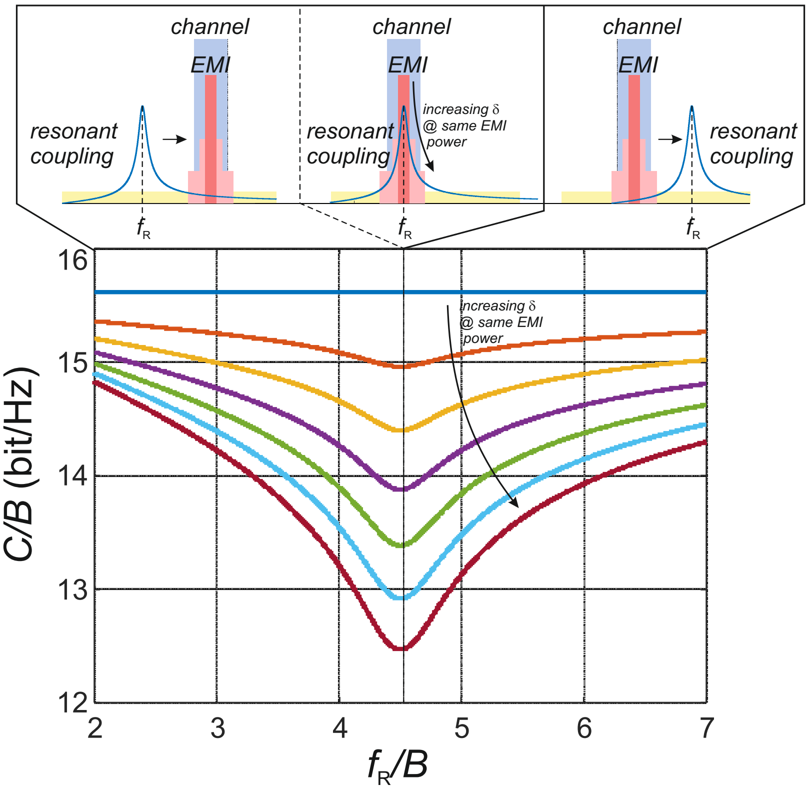

Figure 4. Normalized capacity versus resonant frequency f_R/B for a communication channel with bandwidth $B = (f_1, f_2)$ in the presence of EMI .

For $Q = 1$, the resonant behaviour is weak and the situation is similar to that considered in [37] for wideband EMI coupling (In this study, just the case of EMI bandwidth fully included in the communication channel bandwidth is considered. For extremely narrow-bandwidth communications, EMI coupling can be always considered nearly uniform over the channel bandwidth even in the presence of resonant coupling and the considerations presented in [37] can be directly extended) and an increasing EMI-induced channel capacity loss, weakly dependent on f_R, is observed for an increased SS spreading bandwdith W/B, i.e., for an increased modulation depth δ, which is consistent with [37].

For an increased quality factor Q, the channel capacity loss decreases since the EMI components far from the resonant frequency are partially filtered. Moreover, the capacity loss is more sensitive to the resonant frequency f_R and expectedly reaches a minimum when f_R is close to the EMI central frequency, i.e., for $f_C \simeq f_R$. Even in this case, however, for Q up to 10,000, the EMI-induced capacity loss gets worse and worse by increasing the spreading bandwidth W/B of SS-modulations. A beneficial effect of SS-modulations, which could be possibly expected in view of the reduced SS-EMI coupled power under resonant conditions, as highlighted in Figure 1, is observed only for extremely high Q values exceeding 10,000, where the peak capacity loss decreases for an increasing spreading bandwidth W/B. Even in these cases, for SS-modulations, a capacity impairment is experienced over a wider bandwidth compared to the case with lower W/B or no SS-modulation. Such extremely high values of the quality factor, however, are not realistic for EMI coupling.

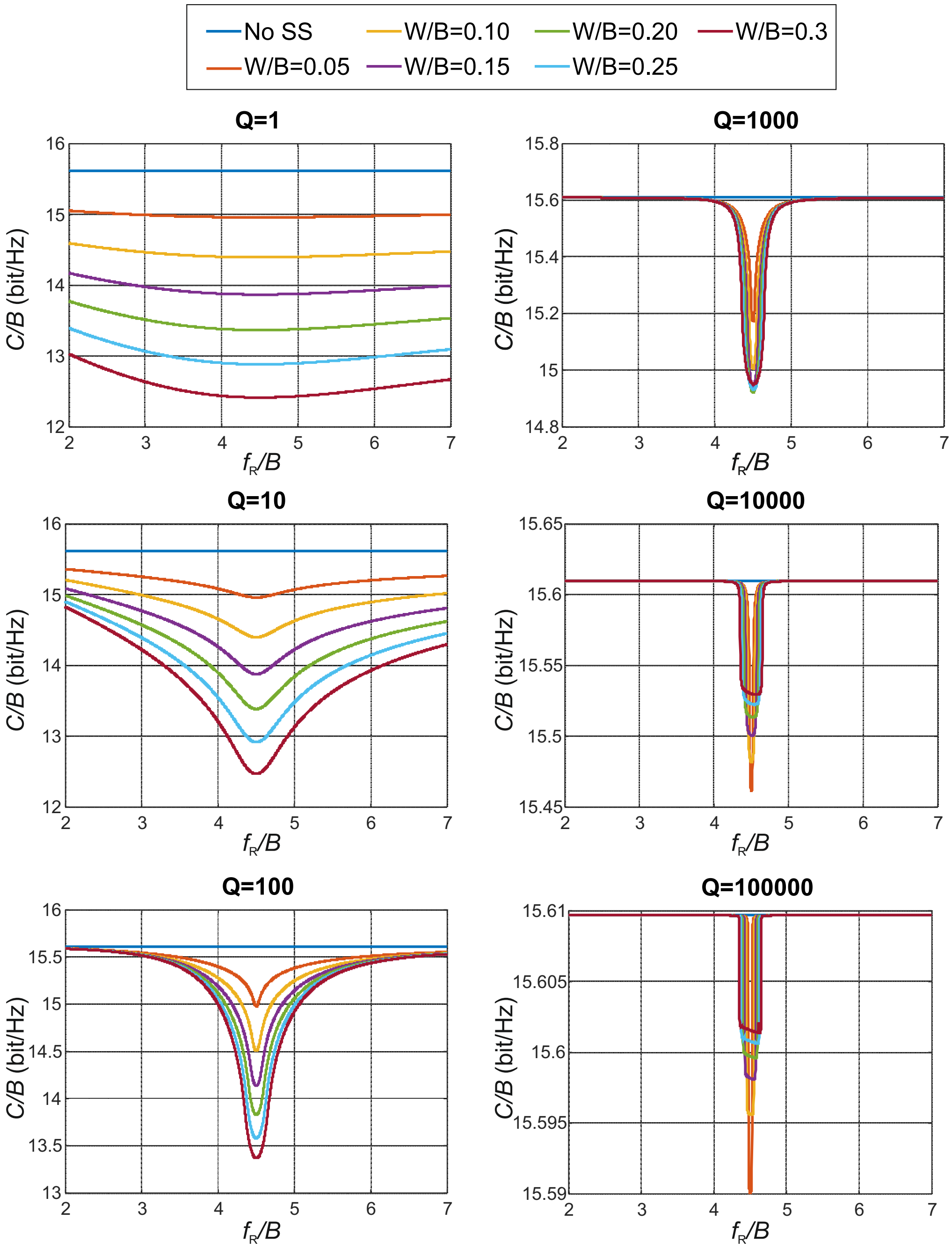

Figure 5. Normalized capacity versus resonant frequency f_R/B for the channel in Figure 3 for different values of the resonant coupling quality factor Q under constant peak coupling, reported in each plot for different SS-modulation depth δ ranging from 0 (no SS) to 30%.

To better highlight the effect of SS-modulations, the worst case channel capacity and the average EMI-induced capacity loss over different values of f_R ranging from $2B$ to $7B$ are reported in Figures 6 and 7, respectively, versus W/B. It can be clearly observed that the worst case capacity monotonically decreases with W/B for practical values of Q below 10,000 and shows an increasing behavior only for extremely high values of Q and for quite large W/B ratios, according to the previous discussion. By contrast, the average channel capacity has found to be monotonically decreasing with W/B for any value of Q.

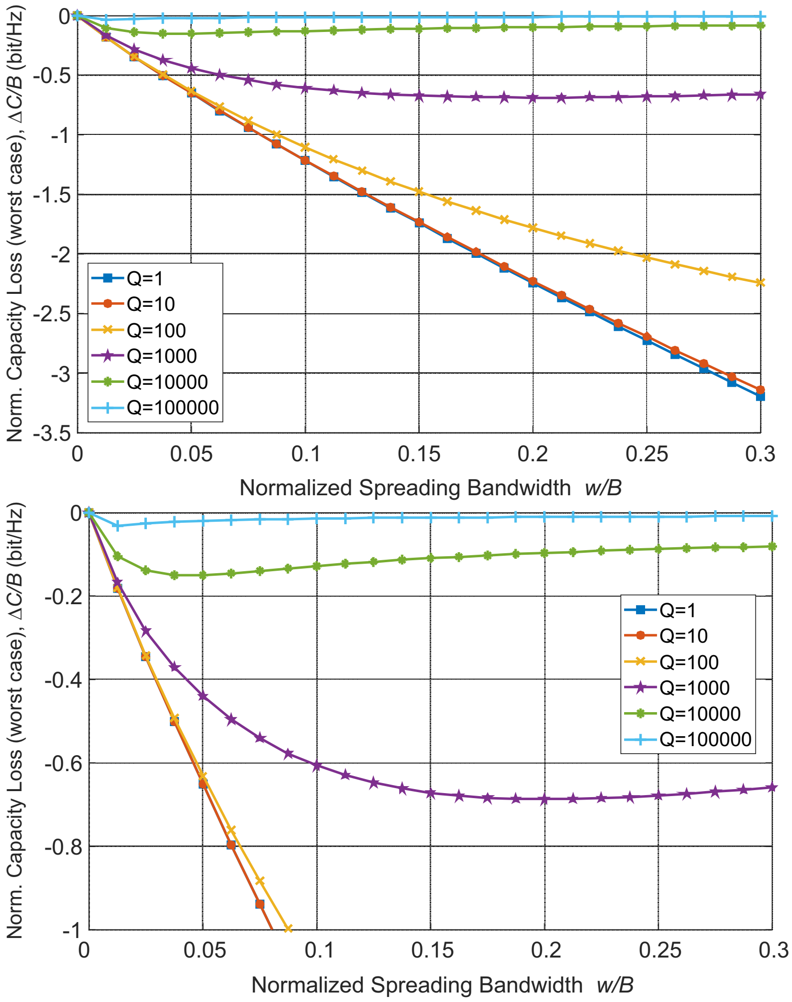

Figure 6. Worst case normalized capacity loss over different resonant frequencies f_{R} versus SS-modulation depth δ ranging from 0 (no SS) to 30% for different values of the resonant coupling quality factor Q under constant peak coupling. A detail of the top figure is reported in the bottom figure.

To further investigate the effect of SS-modulation under resonant coupling, the analysis described above has been repeated choosing the scaling constant G_0 in (3) so that the coupling function $G(f)$ has unitary energy, i.e., imposing

$$\int_{-\infty}^{+\infty} |G(f)|^2 \mathrm{d}f = 1.$$

In analogy with Figures 6 and 7, the average and the worst case capacity loss over different values of f_{R} are reported in Figure 8 versus the SS bandwidth W normalized with respect to the channel bandwidth. In this case, a monotonic decrease of both the average and of the worst case channel capacity is observed for increased W/B for all the considered values of the quality factor Q.

Under the hypotheses and limitations considered in the proposed analysis, i.e., that SS EMI can be described as a band-limited Gaussian random process, which is coupled to a wideband AWGN channel by resonant coupling described by the transfer function (3), it can be observed that the application of SS-modulations on periodic interfering signals gives rise to a larger EMI-induced capacity loss under the same EMI total power compared to non-SS-modulated EMI for almost all practical resonant EMI coupling conditions. In other words, the results on the impact of SS-modulations on EMI-induced capacity loss studied in [37] for wideband EMI coupling can be extended to practical resonant coupling conditions according to the proposed analysis.

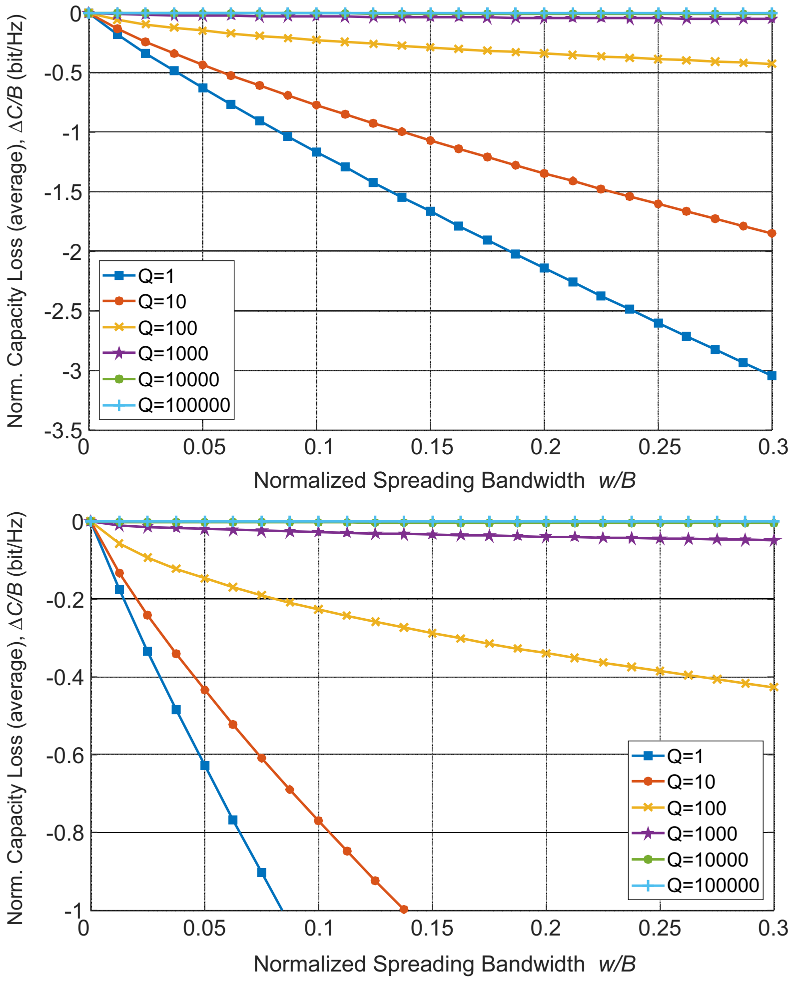

Figure 7. Average normalized capacity for resonant frequencies f_R ranging from $2B$ to $7B$ versus SS-modulation depth δ ranging from 0 (no SS) to 30% for different values of the resonant coupling quality factor Q under constant peak coupling. A detail of the top figure is reported in the bottom figure.

As observed in [37], such a larger capacity loss is not always related to an increased bit error rate (BER) in communication channels operating at sub-capacity bit rates, by the way it is expected to give rise to a worse and worse BER degradation as far as the data rate approaches the Shannon capacity limit, as in real world communication channels employing advanced channel coding schemes (e.g., Turbo coding). Under this perspective, the impact of SS-modulations on the BER of a 4-QAM digital link featuring Turbo coding will be considered as a test case in what follows.

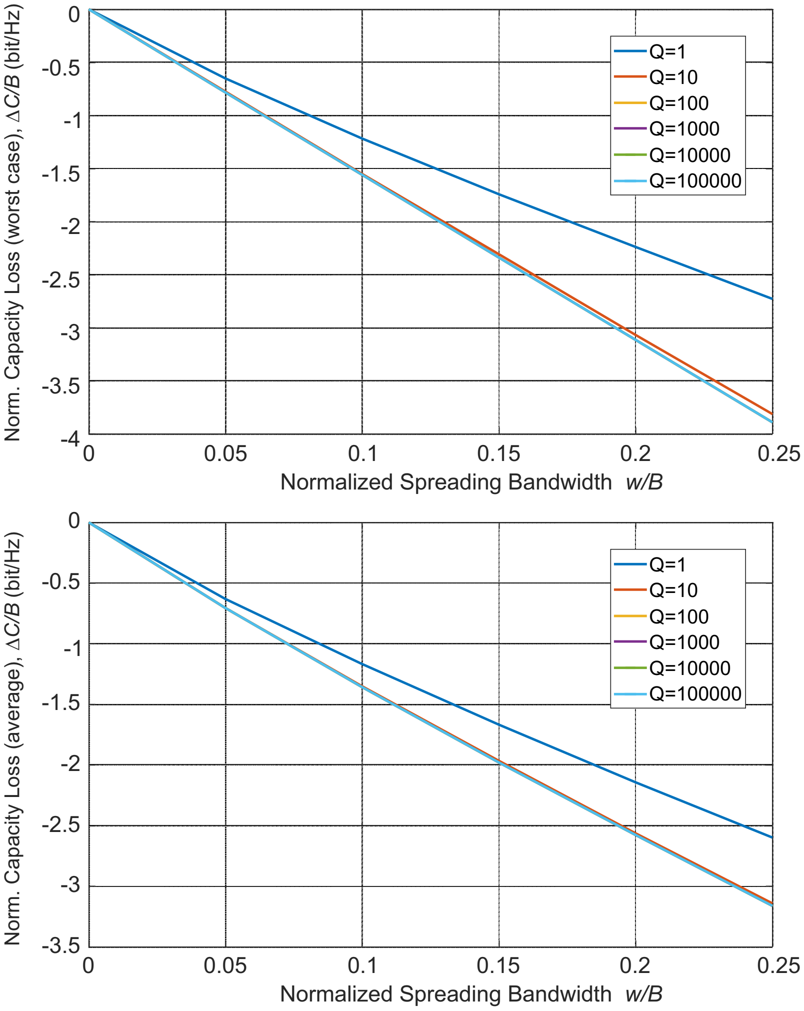

Figure 8. Worst case and average normalized capacity loss over different resonant frequencies f_R versus SS-modulation depth δ ranging from 0 (no SS) to 25% for different values of the resonant coupling quality factor Q under constant coupling integral.

5. Impact of Spread Spectrum Modulations in a 4-QAM Channel under Resonant EMI Coupling

The effects of SS EMI on a communication channel under resonant EMI couping, which have been discussed in the previous section in a completely general, coding-independent way in terms of equivalent channel capacity loss, are now investigated with reference to a synchronous buck DC–DC power converter interfering with a 4-QAM digital link featuring Turbo coding, which makes it possible to achieve a data rate approaching the channel capacity and is therefore expected to be more sensitive to EMI-induced capacity loss [37].

Test Setup

The interference generated by a synchronous buck DC–DC converter has been measured and added in simulation to the input signal of a 4-QAM digital communication channel under resonant coupling with $Q = 1$ and $Q = 100$.

In order to extract the EMI waveforms, the test setup in Figure 9, which is the same presented in [35], is considered. Here, a DC–DC power converter is intentionally designed to interfere with a digital data link. The converter is a hard-switched synchronous Buck operated from an input voltage $V_{IN} = 16$ V and connected to a load $R_L = 10\ \Omega$ in open-loop mode with a fixed duty cycle $D = 0.375$. Such a converter is driven by a 100kHz PWM signal generated by a microcontroller, which can programmed to operate at constant frequency or with an SS random frequency modulation with different modulation depth δ. The EMI voltage v_c at the receiver input without SS-modulation and with random SS-modulation at different modulation depth δ is acquired by a digital scope at 125 MS/s during the DC–DC converter operation and is stored in a database. The power spectral density of the measured waveform for periodic and random SS-modulated ($\delta = 6\%$) is reported in Figure 10.

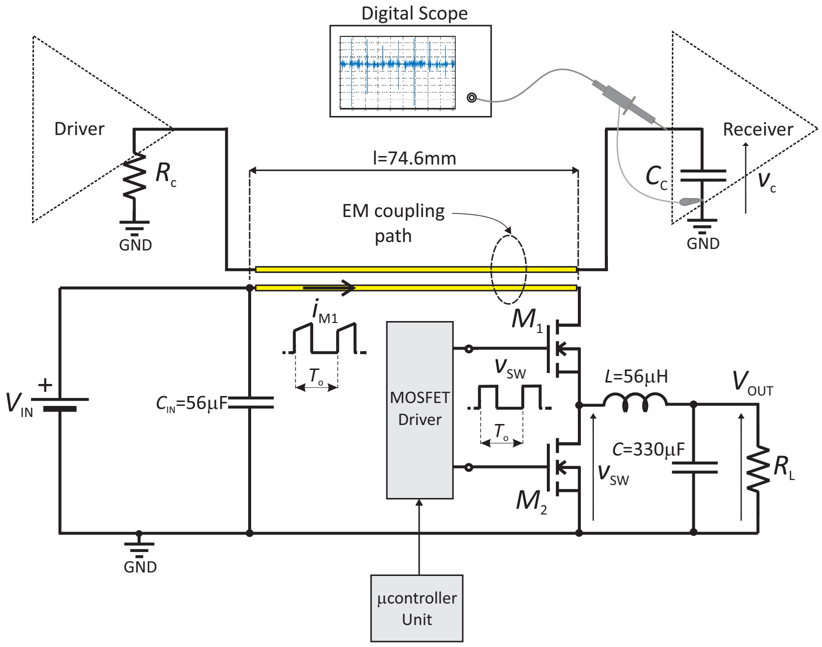

Figure 9. Schematic view of the test setup.

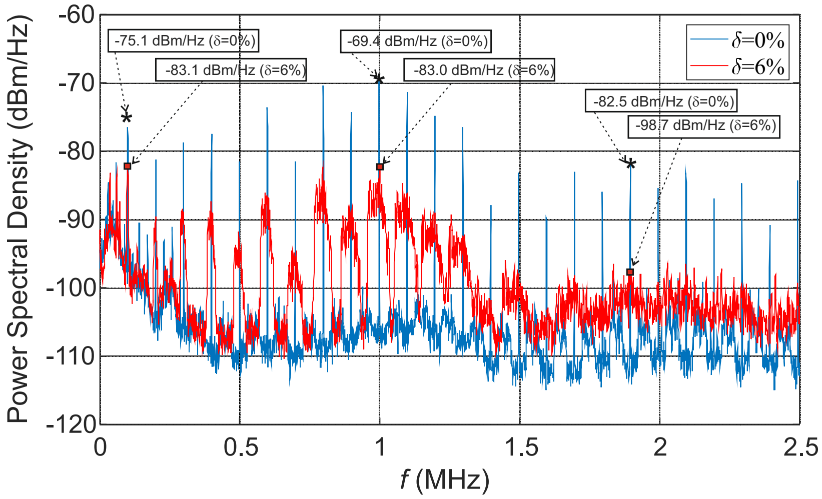

Figure 10. Measured power spectral density of periodic and random SS-modulated ($\delta = 6\%$) EMI.

Then, the measured EMI waveforms are added in simulation to the input of a 4-QAM receiver, modelling the EMI propagation path to the receiver as a resonant transfer function $G(f)$ with $Q = 1$ and $Q = 100$ to discuss the impact of different resonant coupling mechanisms.

For this purpose, a 4-QAM communication scheme over an AWGN channel with $B = 600$ kHz bandwidth is considered and the effects of non-modulated and SS-modulated EMI coupled to the channel bandwidth with a resonant transfer function with $Q = 1$ and with $Q = 100$ have been simulated in the Matlab environment, adding the measured non-modulated and SS-modulated EMI waveforms generated by the power converter to the received input signal.

In Figure 11, resonant coupling with $Q = 1$ is considered and the BER is plotted versus the r.m.s. EMI amplitude (disturbances with different amplitudes have been obtained applying a scaling factor to the same measured EMI waveforms) for different values of the modulation depth δ. From the figure, it can be observed that the EMI amplitude at which BER starts increasing in a significant way is lower for a larger SS-modulation depth and higher in the non-modulated case or for small values of δ.

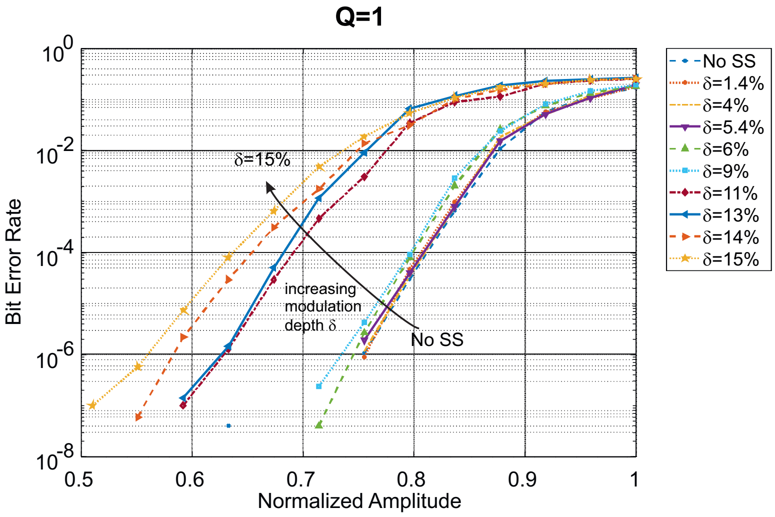

Figure 11. Bit error rate of a communication channel corrupted by SS-modulated EMI under weakly resonant coupling ($Q = 1$) vs. EMI normalized r.m.s. amplitude at different modulation depth δ.

Comparing non-modulated EMI with SS-modulated EMI, a similar BER is achieved for a 20% higher EMI amplitude in the non-modulated case. In Figure 12, the same analysis is performed under resonant EMI coupling with quality factor $Q = 100$. In this case, a similar BER is achieved for a 3.4X higher EMI amplitude than in the non-modulated cases, revealing an even worse impact of SS-modulations on the BER when an EMI resonant coupling with a higher Q factor is introduced.

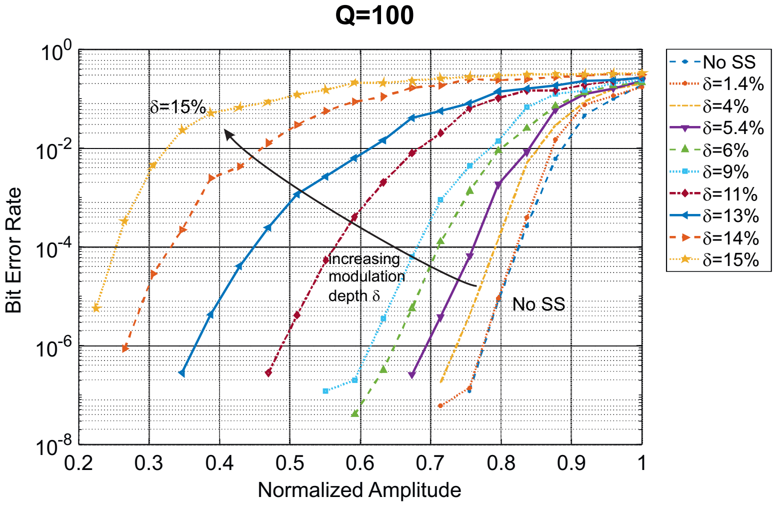

Figure 12. Bit error rate of a communication channel corrupted by SS-modulated EMI under strongly resonant coupling ($Q = 100$) vs. EMI normalized r.m.s. amplitude at different modulation depth δ.

Based on the same analysis described above, the BER has been plotted for different EMI power levels versus the modulation depth δ in Figure 13 for $Q = 1$ and in Figure 14 for $Q = 100$ and also in this case a worse BER degradation with increased SS-modulation depth is observed for resonant coupling with an increased quality factor.

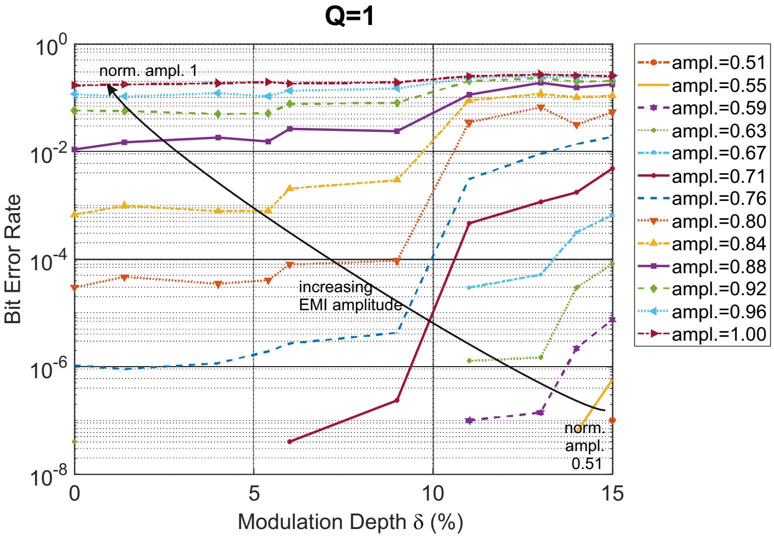

Figure 13. Bit error rate of a communication channel corrupted by SS-modulated EMI under weakly resonant coupling ($Q = 1$) vs. different modulation depth δ at different EMI normalized r.m.s. amplitude values.

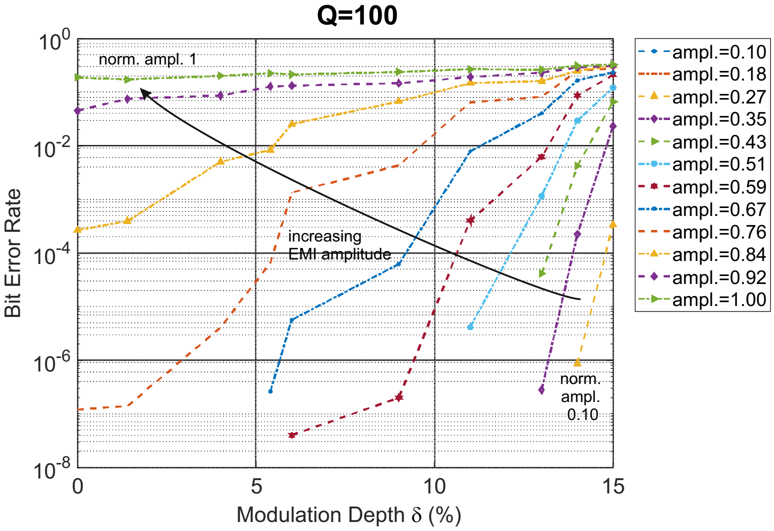

Figure 14. Bit error rate of a communication channel corrupted by SS-modulated EMI under strongly resonant coupling ($Q = 100$) vs. different modulation depth δ at different EMI normalized r.m.s. amplitude values.

6. Conclusions

The effects of EMI coupled to a communication channel by narrowband resonant mechanisms have been investigated in terms of an equivalent channel capacity loss. In this framework, the effects of non-modulated and random SS-modulated EMI under different resonant frequency and quality factors of the EMI coupling mechanism have been compared, thus extending the analysis presented in [37], which was limited to the case of wideband EMI coupling. The analysis has revealed a higher EMI-induced capacity loss for SS-modulated compared to non modulated EMI under practical values of the quality factor Q, while a modest improvement in the worst case capacity loss is observed only for impractical values of Q exceeding 10,000. Simulations on a 4-QAM digital link featuring Turbo coding under EMI resonant coupling have also revealed that SS-modulated EMI gives rise to higher BER at lower EMI power compared WITH non-modulated EMI also in the presence of resonant coupling with practical values, thus confirming a worse interfering potential of SS-modulated EMI.

Author Contributions: Conceptualization, methodology, formal analysis: P.S.C.; validation, writing F.M. All authors have read and agreed to the published version of the manuscript.

Funding: This research received no external funding.

Conflicts of Interest: The authors declare no conflict of interest.

References

1. Dhia, S.B.; Ramdani, M.; Sicard, E. *Electromagnetic Compatibility of Integrated Circuits: Techniques for Low Emission and Susceptibility*; Springer: New York, NY, USA, 2006.
2. Archambeault, B.; Ruehli, A.E. Analysis of power/ground-plane EMI decoupling performance using the partial-element equivalent circuit technique. *IEEE Trans. Electromagn. Compatibil.* **2001**, *43*, 437–445. [CrossRef]
3. Shringarpure, K.; Pan, S.; Kim, J.; Fan, J.; Achkir, B.; Archambeault, B.; Drewniak, J.L. Sensitivity Analysis of a Circuit Model for Power Distribution Network in a Multilayered Printed Circuit Board. *IEEE Trans. Electromagn. Compatibil.* **2017**, *59*, 1993–2001. [CrossRef]
4. Kim, J.; Rotaru, M.D.; Baek, S.; Park, J.; Iyer, M.K.; Kim, J. Analysis of noise coupling from a power distribution network to signal traces in high-speed multilayer printed circuit boards. *IEEE Trans. Electromagn. Compatibil.* **2006**, *48*, 319–330. [CrossRef]
5. Crovetti, P.S. Operational amplifier immune to EMI with no baseband performance degradation. *Electron. Lett.* **2010**, *46*, 209–210. [CrossRef]
6. Redouté, J.; Richelli, A. A methodological approach to EMI resistant analog integrated circuit design. *IEEE Electr. Comp. Mag.* **2015**, *4*, 92–100. [CrossRef]
7. Villavicencio, Y.; Musolino, F.; Fiori, F. Electrical Model of Microcontrollers for the Prediction of Electromagnetic Emissions. *IEEE Trans. Very Large Scale Integr. (VLSI) Syst.* **2011**, *19*, 1205–1217. [CrossRef]
8. 'Code of Federal Regulations, Title 47, Chapter I, Subchapter A, Part 15, Subpart B: Unintentional Radiators'. Available online: https://www.ecfr.gov/ (accessed on 19 July 2018).
9. *Council Directive 89/336/EEC on the Approximation of the Laws of the Member States Relating to Electromagnetic Compatibility*; Official Journal of the European Union, Technical Report L139/19; The Publications Office of the European Union: Luxembourg, 1989.
10. *CISPR 11:2015 Industrial, Scientific and Medical Equipment - Radio-Frequency Disturbance Characteristics—Limits and Methods of Measurement*; IEC: Geneva, Switzerland, 2015.
11. *CISPR 14-1:2016 Electromagnetic Compatibility - Requirements for Household Appliances, Electric Tools and Similar Apparatus—Part 1: Emission*; IEC: Geneva, Switzerland, 2016.
12. Musolino, F.; Villavicencio, Y.; Fiori, F. Chip-Level Design Constraints to Comply With Conducted Electromagnetic Emission Specifications. *IEEE Trans. Electromagn. Compatibil.* **2012**, *54*, 1137–1146. [CrossRef]
13. Crovetti, P.S.; Fiori, F.L. Efficient BEM-based substrate network extraction in silicon SoCs. *Microelectron. J.* **2008**, *39*, 1774–1784. [CrossRef]
14. Lobsiger, Y.; Kolar, J.W. Closed-Loop di/dt and dv/dt IGBT Gate Driver. *IEEE Trans. Power Electron.* **2015**, *30*, 3402–3417. [CrossRef]
15. Chung, H.; Hui, S.Y.R.; Tse, K.K. Reduction of power converter EMI emission using soft-switching technique. *IEEE Trans. Electromagn. Compatibil.* **1998**, *40*, 282–287. [CrossRef]
16. Pareschi, F.; Rovatti, R.; Setti, G. EMI Reduction via Spread Spectrum in DC/DC Converters: State of the Art, Optimization, and Tradeoffs. *IEEE Access* **2015**, *3*, 2857–2874. [CrossRef]
17. Lin, F.; Chen, D.Y. Reduction of power supply EMI emission by switching frequency modulation. *IEEE Trans. Power Electron.* **1994**, *9*, 132–137.
18. Hardin, K.B.; Fessler, J.T.; Bush, D.R. Spread spectrum clock generation for the reduction of radiated emissions. In Proceedings of the IEEE Symposium on Electromagnetic Compatibility, Chicago, IL, USA, 22–26 August 1994; pp. 227–231.
19. Chen, Y.; Ma, D.B. 15.7 An 8.3MHz GaN Power Converter Using Markov Continuous RSSM for 35dBμV Conducted EMI Attenuation and One-Cycle TON Rebalancing for 27.6dB VO Jittering Suppression. In Proceedings of the 2019 IEEE International Solid- State Circuits Conference—(ISSCC), San Francisco, CA, USA, 17–21 February 2019; pp. 250–252.

20. De Martino, M.; De Caro, D.; Esposito, D.; Napoli, E.; Petra, N.; Strollo, A.G.M. A Standard-Cell-Based All-Digital PWM Modulator With High Resolution and Spread- Spectrum Capability. *IEEE Trans. Circuits Syst. I Regul. Pap.* **2018**, *65*, 3885–3896. [CrossRef]
21. Jun, J.; Bae, S.; Lee, Y.; Kim, C. A Spread Spectrum Clock Generator With Nested Modulation Profile for a High-Resolution Display System. *IEEE Trans. Circuits Syst. II Express Briefs* **2018**, *65*, 1509–1513. [CrossRef]
22. De Caro, D.; Tessitore, F.; Vai, G.; Imperato, N.; Petra, N.; Napoli, E.; Parrella, C.; Strollo, A.G. A 3.3 GHz Spread-Spectrum Clock Generator Supporting Discontinuous Frequency Modulations in 28 nm CMOS. *IEEE J. Solid-State Circuits* **2015**, *50*, 2074–2089. [CrossRef]
23. Hwang, S.; Song, M.; Kwak, Y.; Jung, I.; Kim, C. A 3.5 GHz Spread-Spectrum Clock Generator With a Memoryless Newton-Raphson Modulation Profile. *IEEE J. Solid-State Circuits* **2012**, *47*, 1199–1208. [CrossRef]
24. *Spread Spectrum Clocking Using the CDCS502/503*; Application Note SCAA103; Texas Instruments: Dallas, TX, USA, 2009.
25. *STM32 MCUs Spread-Spectrum Clock Generation Principles, Properties and Implementation*; Application Note AN4850; STMicroelectronics: Geneva, Switzerland, 2016.
26. *R1275S Series, 30V, 2A, Synchronous PWM Step-Down DC/DC Converter*; Ricoh Electronic Devices Co. Ltd.: Tokyo, Japan, 2018.
27. Multiphase Oscillator with Spread Spectrum Frequency Modulation, Document LTC6902, Linear Technology, 2003. Available online: http://cds.linear.com/docs/en/datasheet/6902f.pdf (accessed on 19 December 2019).
28. Callegari, S.; Rovatti, R.; Setti, G. Spectral properties of chaos-based FM signals: theory and simulation results. *IEEE Trans. Circuits Syst. I Fundament. Theory Appl.* **2003**, *50*, 3–15. [CrossRef]
29. Setti, G.; Balestra, M.; Rovatti, R. Experimental verification of enhanced electromagnetic compatibility in chaotic FM clock signals. In Proceedings of the 2000 IEEE International Symposium on Circuits and Systems (ISCAS), Geneva, CH, 28–31 May 2000; Volume 3, pp. 229–232.
30. KTse, K.; Chung, H.S.; Hui, S.Y.R.; So, H.C. A comparative study of carrier-frequency modulation techniques for conducted EMI suppression in PWM converters. *IEEE Trans. Ind. Electron.* **2002**, *49*, 618–627.
31. Lauder, D.; Moritz, J. *Investigation into Possible Effects Resulting From Dithered Clock Oscillators on EMC Measurements and Interference to Radio Transmission Systems*; Radiocommunications Agency: London, UK, March 2000.
32. Hardin, K.; Oglesbee, R.A.; Fisher, F. Investigation into the interference potential of spread-spectrum clock generation to broadband digital communications. *IEEE Trans. Electromagn. Compatibil.* **2003**, *45*, 10–21. [CrossRef]
33. Mukherjee, R.; Patra, A.; Banerjee, S. Impact of a Frequency Modulated Pulsewidth Modulation (PWM) Switching Converter on the Input Power System Quality. *IEEE Trans. Power Electron.* **2010**, *25*, 1450–1459. [CrossRef]
34. Skinner, H.; Slattery, K. Why spread spectrum clocking of computing devices is not cheating. In Proceedings of the 2001 IEEE EMC International Symposium. Symposium Record. International Symposium on Electromagnetic Compatibility (Cat. No.01CH37161), Montreal, QC, Canada, 13–17 August 2001.
35. Musolino, F.; Crovetti, P.S. Interference of Spread-Spectrum Switching-Mode Power Converters and Low-Frequency Digital Lines. In Proceedings of the 2018 IEEE International Symposium on Circuits and Systems (ISCAS), Florence, Italy, 27–30 May 2018; pp. 1–5.
36. Matsumoto, Y.; Shimizu, T.; Murakami, T.; Fujii, K.; Sugiura, A. Impact of Frequency-Modulated Harmonic Noises From PCs on OFDM-Based WLAN Systems. *IEEE Trans. Electromagn. Compatibil.* **2007**, *49*, 455–462. [CrossRef]
37. Musolino, F.; Crovetti, P.S. Interference of Spread-Spectrum Modulated Disturbances on Digital Communication Channels. *IEEE Access* **2019**, *7*, 158969–158980. [CrossRef]
38. Shim, H.; Hubing, T.H. A closed-form expression for estimating radiated emissions from the power planes in a populated printed circuit board. *IEEE Trans. Electromagn. Compatibil.* **2006**, *48*, 74–81. [CrossRef]
39. Zeeff, T.M.; Hubing, T.H. Reducing power bus impedance at resonance with lossy components. *IEEE Trans. Adv. Pack.* **2002**, *25*, 307–310. [CrossRef]
40. Grassi, F.; Spadacini, G.; Marliani, F.; Pignari, S.A. Use of Double Bulk Current Injection for Susceptibility Testing of Avionics. *IEEE Trans. Electromagn. Compatibil.* **2008**, *50*, 524–535. [CrossRef]

41. Crovetti, P.S.; Fiori, F. Distributed Conversion of Common-Mode Into Differential-Mode Interference. *IEEE Trans. Microw. Theory Tech.* **2011**, *59*, 2140–2150. [CrossRef]
42. Crovetti, P.S. Finite Common-Mode Rejection in Fully Differential Nonlinear Circuits. *IEEE Trans. Circuits Syst. II Express Briefs* **2011**, *58*, 507–511. [CrossRef]
43. Shannon, C.E. A Mathematical Theory of Communication. *Bell Syst. Tech. J.* **1948**, *27*, 379–423. [CrossRef]